Breathless BEARS: [Oiii] 88µm emission of dusty star-forming galaxies at z = 3−4

Citation for the original published paper (version of record):

Bakx, T., Algera, H., Prajapati, P. et al (2026). Breathless BEARS: [Oiii] 88µm emission of dusty star-forming galaxies at z = 3−4. Monthly Notices of the Royal Astronomical Society, 546(3). http://dx.doi.org/10.1093/mnras/stag106

Monthly Notices
of the
ROYAL ASTRONOMICAL SOCIETY

MNRAS **546**, 1–8 (2026) https://doi.org/10.1093/mnras/stag106
Advance Access publication 2026 January 16

Breathless BEARS: [O III] 88 μm emission of dusty star-forming galaxies at $z = 3$–4

T. J. L. C. Bakx,[1★] Hiddo S. B. Algera,[2] Prachi Prajapati,[3,4] George Bendo,[5] Stefano Berta,[6] Laura Bonavera,[7,8] Pierre Cox,[9] Joaquin González-Nuevo,[7,8] Masato Hagimoto,[10] Kevin Harrington,[11,12,13,14] Matthew Lehnert,[9,15] Stephen Serjeant,[16] Pasquale Temi,[17] Paul van der Werf,[18] Chentao Yang[1] and Gianfranco De Zotti[19]

Affiliations are listed at the end of the paper

Accepted 2026 January 14. Received 2026 January 14; in original form 2025 December 5

ABSTRACT

We present [O III] 88 μm observations towards four *Herschel*-selected dusty star-forming galaxies (DSFGs; $\log_{10}\mu L_{\rm IR}/L_\odot = 13.5$–14 at $z = 2.9$–4) using the Atacama Compact Array (ACA) in Bands 9 and 10. We detect [O III] emission in all four targets at $> 3\sigma$, finding line luminosity ratios ($L_{\rm [O_{III}]}/L_{\rm IR} = 10^{-4.2}$ to 10^{-3}) similar to local spiral galaxies, and an order of magnitude lower when compared with local dwarf galaxies as well as high-redshift Lyman-break galaxies. Using the short-wavelength capabilities of the ACA, these observations bridge the populations of galaxies with [O III] emission at low redshift from space missions and at high redshift from ground-based studies. The difference in [O III] emission between these DSFGs and other high-redshift galaxies reflects their more evolved stellar populations (>10 Myr), larger dust reservoirs ($M_{\rm dust} \sim 10^{9-11}$ M$_\odot$), metal-rich interstellar medium ($Z \sim 0.5$–2 Z$_\odot$), and likely weaker ionization radiation fields. Ancillary [C II] emission on two targets provide $L_{\rm [O\,III]}/L_{\rm [C\,II]}$ ratios at 0.3–0.9, suggesting that ionized gas represents a smaller fraction of the total gas reservoir in DSFGs, consistent with theoretical models of DSFGs as transitional systems between gas-rich, turbulent disks and more evolved, gas-poor galaxies. Expanding samples of DSFGs with [O III] emission will be key to place this heterogeneous, poorly understood galactic phase in its astrophysical context.

Key words: galaxies: high-redshift – galaxies: ISM – submillimetre: galaxies.

1 INTRODUCTION

Dusty star-forming galaxies (DSFGs) are the most active star-forming galaxies in the Universe (A. W. Blain et al. 2002; C. M. Casey, D. Narayanan & A. Cooray 2014). With total infrared luminosities exceeding 10^{12} L$_\odot$, DSFGs reach the limit of 'maximum starburst' with star-formation rates of 1000 M$_\odot$ yr^{-1} or more (e.g. R. Neri et al. 2020). Compared to local ultra-luminous infrared galaxies, DSFGs are at least one order of magnitude more numerous and contribute strongly to the cosmic star-formation history (P. Madau & M. Dickinson 2014; J. A. Zavala et al. 2021). Their exact nature remains debated (D. Narayanan et al. 2015; C. C. Lovell et al. 2021), and although many are probably mergers (L. J. Tacconi et al. 2008; T. J. L. C. Bakx et al. 2024c), clues to the origins of this galaxy phase can be found through the detailed characterization across multiple phases of the interstellar medium (ISM; C. L. Carilli & F. Walter 2013; J. A. Hodge & E. da Cunha 2020).

Recent comprehensive studies of the molecular and neutral phases have revealed significant insights into their ISM properties. At high densities and lower ionization states, observations of dust, CO, [C I], and [C II] have shown near-constant dust-to-gas ratios (M. Hagimoto et al. 2023), strong variations in gas depletion time-scales (S. Berta et al. 2023; T. J. L. C. Bakx et al. 2024c; P. Prajapati et al. 2026), diverse CO spectral line energy distributions (H. Dannerbauer et al. 2009; E. Daddi et al. 2015; K. C. Harrington et al. 2021), and complex morphologies and kinematics (J. A. Hodge et al. 2019; F. Rizzo et al. 2020, 2024; T. Tsukui et al. 2024). These studies demonstrate that DSFGs represent a dusty phase of galaxy evolution but are not a homogeneous population, with orders-of-magnitude differences in gas densities and properties (T. J. L. C. Bakx et al. 2024a; P. Prajapati et al. 2026).

Characterizing the varying ISM conditions in this diverse population requires large samples of DSFGs. The *Herschel Space Observatory* increased the number of known DSFGs from thousands (e.g. J. M. Simpson et al. 2019; I. Smail et al. 2021) to hundreds of thousands through surveys such as H-ATLAS (S. Eales et al. 2010; E. Valiante et al. 2016; S. J. Maddox et al. 2018; B. A. Ward et al. 2022) and *Herschel* PEP/HerMES (S. J. Oliver et al. 2012). Major progress in the past decade includes the development of large DSFG samples with robust redshifts through spectroscopic surveys (C. Reuter et al. 2020; P. Cox et al. 2023). The Bright Extragalactic ALMA Redshift Survey (BEARS) exemplifies this approach, conducting ALMA observations of 85 DSFGs to mea-

---

★ E-mail: tom.bakx@chalmers.se

sure spectroscopic redshifts (S. A. Urquhart et al. 2022), study field multiplicities (J. A. Hodge et al. 2013; A. Karim et al. 2013), characterize dust spectral energy distributions (G. J. Bendo et al. 2023), and model ISM conditions (M. Hagimoto et al. 2023). These redshift surveys now enable targeted spectral line studies to explore all phases of the ISM systematically.

However, one crucial component of the ISM remains woefully unexplored: the higher ionization states and densities within these systems (P. P. der Werf et al. 2010; M. Rybak et al. 2022; K. C. Harrington et al. 2025). DSFGs' dusty nature precludes consistent optical follow-up through traditional ionization diagnostics (cf. I. Shivaei et al. 2018), leaving fundamental questions about their star-formation processes unanswered, even with the discerning power of the *James Webb Space Telescope* (J. A. Hodge et al. 2025; F. Sun et al. 2025). The submillimeter line of doubly ionized oxygen, [O III] 88 μm, is emitted close to the center of H II regions and serves as an excellent probe of metallicity (L. Vallini et al. 2015; K. Olsen et al. 2017), gas density (A. Ferrara et al. 2019), and ionization parameter (Y. Harikane et al. 2020). Unfortunately, atmospheric transmission precludes ground-based observations of [O III] 88 μm for galaxies in the local Universe out to Cosmic Noon ($z \sim 2$–4; C. Ferkinhoff et al. 2010), and instead current samples of dusty starbursts with [O III] observations are dominated by distant systems ($z \gtrsim 6$) with incidental follow-up (e.g. A. K. Inoue et al. 2016; D. P. Marrone et al. 2018; Y. Tamura et al. 2019; K.-i. Tadaki et al. 2022; S. Schouws et al. 2025a; H. S. B. Algera et al. 2024b; S. Carniani et al. 2025; R. Decarli & T. Díaz-Santos 2025). Despite Cosmic Noon representing the peak epoch for both cosmic star-formation rate density and active galactic nucleus (AGN) activity, seeing to the formation of half of all present-day stars (P. Madau & M. Dickinson 2014), benchmarks of the ionization conditions in the most star-forming galaxies during this period remain sparse and incomplete.

Here, we present [O III] 88 μm observations of four bright southern *Herschel*-selected submillimetre galaxies at $z = 3$–4 using the Atacama Compact Array (ACA) or 'Morita Array', significantly adding to the available data at cosmic noon. This study represents the first systematic survey of [O III] emission in gravitationally lensed DSFGs, providing crucial constraints on the ionized medium properties during the peak epoch of cosmic star formation.[1]

2 SAMPLE, OBSERVATIONS, AND LINE FLUXES

We selected our targets from the complete sample of 72 luminosity-limited *Herschel*-detected DSFGs with robust spectroscopic redshifts from the BEARS survey (S. A. Urquhart et al. 2022). Initially selected from the H-ATLAS survey (S. Eales et al. 2010; E. Valiante et al. 2016), the BEARS sources are all *Herschel* sources in the South Galactic Pole field with S_{500} >80 mJy and the characteristic red submillimeter colours (250, 350, and 500 μm; E. A. Pearson et al. 2013) consistent with $z > 2$ (T. J. L. C. Bakx et al. 2018, 2020b). Our selection was constrained by the requirement that [O III] 88 μm falls within favourable atmospheric windows for ACA observations. Of the 72 sources, 10 galaxies have redshifts between 2.9 and 4.0 that place [O III] in optimal atmospheric transmission windows. The bright far-infrared luminosities ($\log \mu L_{\rm IR}/{\rm L}_\odot = 13.5$–14.0; T. J. L. C. Bakx et al. 2018, 2020b) derived from *Herschel* fluxes enable the ACA to achieve detections, or deep limits, on the oxygen-to-infrared luminosities within 'reasonable' (∼8–10 h per target) observation times.

The availability of nearby calibrators and the necessity for good weather conditions restricted the final sample with [O III] 88 μm observations to four DSFGs (HerBS-28, -90, -103, and -160), with one additional source (HerBS-14) having observations with noisy phase calibration data. Within specific redshift shells with good atmospheric transparency, this selection provides a relatively unbiased view on the brightest DSFGs.

The ACA observations (2023.1.00750.S; P.I. Tom Bakx) were taken between November 2023 and September 2024 in conditions with precipitable water vapours of 0.15–1.01 mm, with the full details in Table A1. The DSFGs HerBS-28, -90, and -160 were observed using Band 9 (A. M. Baryshev et al. 2015), and the DSFG HerBS-103 using Band 10 (Y. Uzawa et al. 2013), with the [O III] line centred on one of the spectral windows within one of the sidebands while ensuring the best possible atmospheric transmission in the other sideband. The data cubes were produced using the pipeline SCRIPTFORPI.PY and CASA version 6.6.0 (CASA Team 2022) TCLEAN procedure with a natural weighting and the Hogbom deconvolver (J. A. Högbom 1974). The resulting per-bin sensitivity of the data cubes is between 6 and 13 mJy in 35 km s^{-1} bins with beam sizes ranging between 0.65 and 1.9 arcsec, also including a 10 per cent flux uncertainty based on the ALMA Technical Handbook (A. Remijan et al. 2019).

We detect the underlying dust continuum at $> 15\sigma$ in all four sources. These ACA continuum fluxes are consistent within 20 per cent of the *Herschel* SPIRE 350 and 500 μm (860 and 600 GHz, respectively) measurements that probe similar observed-frame frequencies, confirming that no significant flux is lost in the ACA observations while revealing no source multiplicity. Since their inclusion in dust continuum modelling does not significantly improve the $L_{\rm IR}$ estimates previously established in T. J. L. C. Bakx et al. (2018, 2020b), we use the established $L_{\rm IR}$ values while continuum-subtracting the data cubes to explore the line emission.

Line fluxes are extracted using the procedure detailed in T. J. L. C. Bakx et al. (2024c) and summarized in Table 1. We show their continuum-subtracted lines in Fig. 1. In short, an aperture is created that best matches the expected emission based on ancillary data. In this case, we use higher resolution 0.1 arcsec Band 7 data from the ANGELS program [T. J. L. C. Bakx et al. 2024c and Bakx et al. (in preparation)] where the dust continuum of the sources is strongly detected ($> 20\sigma$). These continuum data are then smoothed to the resolution of the [O III] data cube. Using the average beam of the data cube, the aperture is widened by a beam if the signal-to-noise ratio permitted[2] to ensure extended flux is also included in the flux measurement.

The line-integrated (i.e. moment-0) maps show $>3\sigma$ [O III] 88 μm emission for all four sources. Since the redshifts are determined robustly from multiple CO lines, quantify without ext

---

[1] Throughout this letter, we assume a flat Λ-cold dark matter cosmology with the best-fitting parameters derived from the *Planck* results (Planck Collaboration VI 2020), which are $\Omega_{\rm m} = 0.315$, $\Omega_\Lambda = 0.685$, and $h = 0.674$.

[2] Indicated by $N_{\rm beam}$ in Fig. 1; the extent of subsequent smoothing is decided on a per-source basis, ensuring no significant flux is missed but also minimizing the additional noise that comes from an aperture that is too large.

Table 1. Sample and line properties of the $z = 3$–4 DSFG sample.

Source	z	RA (hms)	Dec. (dms)	$S_{[\mathrm{O\,III}]}dV$ (Jy km s^{-1})	FWHM$_{[\mathrm{O\,III}]}$ (km s^{-1})	$L_{[\mathrm{O\,III}]}$ (10^9 L$_\odot$)	$S_{[\mathrm{C\,II}]}dV$ (Jy km s^{-1})	FWHM$_{[\mathrm{C\,II}]}$ (km s^{-1})	$L_{[\mathrm{C\,II}]}$ (10^9 L$_\odot$)	$L_{[\mathrm{O\,III}]}/L_{[\mathrm{C\,II}]}$
HerBS-28	3.925	23:08:15.76	−34:38:00.3	5.6 ± 1.5	*600*	5.2 ± 1.5	33.6 ± 8.2	601 ± 111	18.8 ± 4.2	0.3 ± 0.1
HerBS-90	3.992	00:56:59.27	−29:50:39.7	5.7 ± 3.4	364 ± 163	5.4 ± 3.2	–	–	–	–
HerBS-103	2.942	22:53:24.23	−32:35:04.3	12.3 ± 2.7	576 ± 128	7.1 ± 1.6	26.0 ± 7.3	669 ± 144	8.5 ± 2.3	0.9 ± 0.3
HerBS-160	3.955	01:10:14.46	−31:48:16.2	8.3 ± 3.5	297 ± 96	5.6 ± 2.2	–	–	–	–

Note. Col. 1: Source name. Col. 2: Redshift based on CO observations (S. A. Urquhart et al. 2022). Col. 3 and 4: RA and Dec. positions from high-resolution observations. Col. 5, 6, and 7: [O III] 88 μm velocity integrated line fluxes, line widths, and luminosities. Limits are shown at 3σ. Italics indicate a fixed line width based on the [C II] 158 μm width. Col. 8, 9, and 10: [C II] 158 μm velocity integrated line fluxes, line widths, and luminosities for the two sources where these are available. Col. 11: The $L_{[\mathrm{O\,III}]}/L_{[\mathrm{C\,II}]}$ line luminosity ratio.

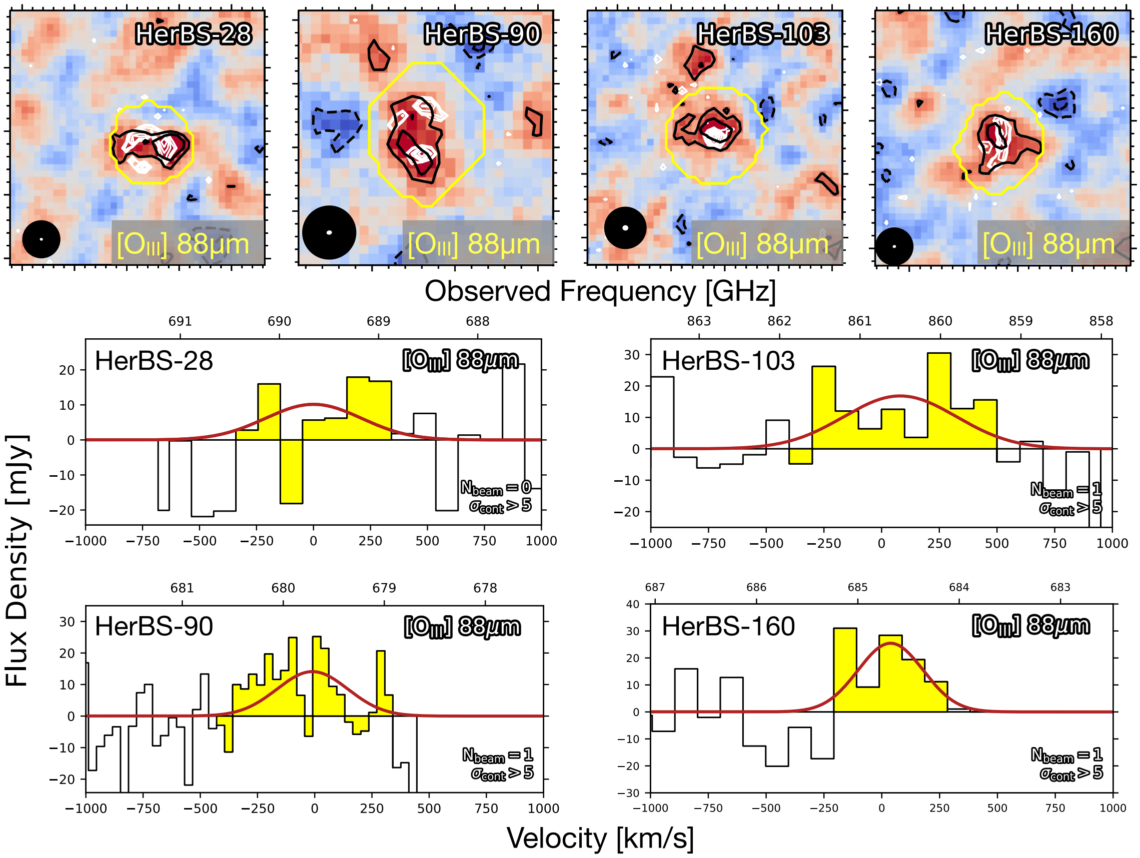

Figure 1. The spectra of the [O III] emission line of HerBS-28, -90, -103, and -160. The poststamps shows the 12 arcsec by 12 arcsec moment-0 map of the [O III] 88 μm emission line as the background and black solid (positive) and dashed (negative) contours at 2σ, 3σ, 5σ starting at ±2, centred on the positions listed in Table 1. The white contour indicates the high-resolution Band 7 continuum data (T. J. L. C. Bakx et al. 2024c), which is used as the basis for the aperture as shown in *yellow contours*. This aperture uses the 5σ continuum flux contours and is subsequently extended by a number of beams (N_{beam}) to capture most of the line flux without diluting the signal with excess noise. The spectra show the emission line as a function of velocity (bottom x-axis) and frequency (top x-axis), where the *filled yellow region* indicates the range over which the moment-0 map is generated, and the *red solid line* indicates a single-Gaussian fit to the line profile.

ensive, resolved observatthis provides confidence in the veracity of these lines. The spectra for HerBS-28 and -103 were noisy, so a lower resolution data cube was produced with 100 km s^{-1} bins. For all but HerBS-28, a Gaussian line fit subsequently measures the velocity-integrated line flux and line width. For HerBS-28, the line velocity width was fixed to the line width from ancillary [C II] 158 μm measurements in order to constrain the fit. The line luminosities are calculated using the equations given in P. M. Solomon & P. A. Vanden Bout (2005). Two of the sources, HerBS-28 and -103, have ancillary [C II] observations (2021.1.00265.S; P.I. Dominik Riechers). These data have been processed in the same fashion as the [O III] observations and are also detailed in Table 1 and Fig. B1.

3 IMPLICATIONS

Our ACA observations resulted in four [O III] 88 μm detections with velocity-integrated line fluxes between 5.6 and 13 Jy km s^{-1} and line luminosities ranging from 5 to 10 × 10^9 L$_\odot$. Fig. 2 shows the [O III]-to-infrared luminosity ratio of our DSFGs against their

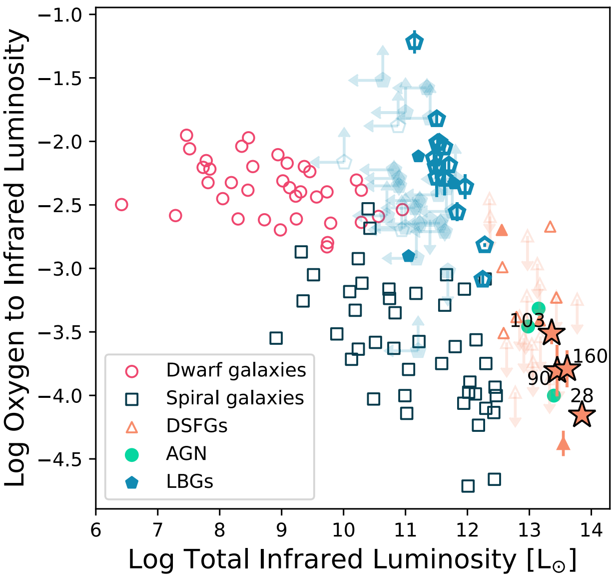

Figure 2. The [O III]-to-IR luminosity ratio as a function of IR luminosity. The open circles (dwarf galaxies; S. C. Madden et al. 2013; D. Cormier et al. 2015; P. Cigan et al. 2016; R. Ura et al. 2023) and squares (local spiral galaxies; C. Ferkinhoff et al. 2010; R. Herrera-Camus et al. 2018) represent low-redshift galaxies. High-redshift galaxies are shown in open (T. J. L. C. Bakx et al. 2024b) and filled pentagons for Lyman-Break Galaxies (LBGs; A. K. Inoue et al. 2016; N. Laporte et al. 2017; S. Carniani et al. 2017; T. Hashimoto et al. , 2019; S. Schouws et al. 2022; H. B. Akins et al. 2022; T. J. L. C. Bakx et al. 2023; Y. W. Ren et al. 2023; H. S. B. Algera et al. 2024a; S. Fujimoto et al. 2024; S. Schouws et al. 2025a; J. A. Zavala et al. 2024; S. Carniani et al. 2025), with AGNs shown in filled circles (T. Hashimoto et al. 2019; R. Decarli et al. 2023) and distant DSFGs in open (Z.-Y. Zhang et al. 2018) and filled triangles (D. P. Marrone et al. 2018; J. A. Zavala et al. 2018; K.-i. Tadaki et al. 2022).

infrared luminosity, comparing these to the established [O III]-to-infrared luminosity ratios from local dwarf irregular galaxies and spiral galaxies. Our detected DSFGs systematically fall in the regime of star-forming spiral galaxies, with [O III]-to-infrared luminosity ratios ranging from $10^{-4.2}$ to 10^{-3}. LBGs at higher redshifts typically show $L_{[\rm O\,III]}/L_{\rm IR}$ ratios consistent with or slightly elevated above local dwarf galaxies, while these $z > 2$ DSFGs appear to be [O III]-faint for $z > 1$ galaxies.

Fig. 3 shows the $L_{[\rm O\,III]}/L_{[\rm C\,II]}$ ratio as a function of redshift. Using [C II] measurements from ancillary ALMA observations, the $L_{[\rm O\,III]}/L_{[\rm C\,II]}$ ratio of HerBS-28 is 0.3 ± 0.1 and of HerBS-103 is 0.9 ± 0.3. These ratios are significantly lower than those typically observed in high-redshift LBGs (1–10; e.g. H. S. B. Algera et al. 2024a), instead suggesting weaker ionization parameters ($U \sim 10^{-3}$ to $10^{-2.5}$) compared to typical LBGs ($U \sim 10^{-2}$ to $10^{-1.5}$; Y. Harikane et al. 2020). In these DSFGs with high infrared surface brightnesses (M. Hagimoto et al. 2023; T. J. L. C. Bakx et al. 2024c), the fraction of [C II] emission arising from neutral photo-dissociation regions typically exceeds 80 per cent (e.g. T. Díaz-Santos et al. 2017). In such environments, the [C II] line is dominated by the neutral gas reservoir rather than the ionized H II regions from where [O III] originates, naturally resulting in the lower observed line ratios compared to less-obscured, high-redshift LBGs. This indicates that the ionized gas phase represents a smaller fraction of the total gas reservoir in DSFGs compared to typical star-forming galaxies. This is consistent with the large reservoirs of molecular gas of DSFGs, and in line with recent studies of [C II]-selected companion galaxies to quasars (T. J. L. C. Bakx et al. 2024b; I. F. Leeuwen et al. 2025).

Observationally, it appears that low [O III]-to-infrared luminosity ratios are driven by enhanced metallicities (T. Hashimoto et al. 2019; Y. Tamura et al. 2019). Given their large gas masses and high infrared luminosities, DSFGs likely harbour more evolved stellar populations with ages in excess of >50 Myr (S. Berta et al. 2023), while younger LBGs appear to have bursty star formation (L. Vallini et al. 2021) and younger stellar populations (∼4 Myr; e.g. Y. Tamura et al. 2019). Furthermore, the high dust-to-gas mass ratios of DSFGs appear to indicate (near-)solar metallicities ($Z \sim 0.5$–$2\ {\rm Z}_\odot$; M. Hagimoto et al. 2023; P. Prajapati et al. 2026), while typically LBGs have more modest metallicities (K. Nakajima et al. 2023; cf. L. E. Rowland et al. 2026) and dust masses (H. Inami et al. 2022), in part due to their UV selection. This interpretation is in line with the elevated $L_{[\rm O\,III]}/L_{[\rm C\,II]}$ ratios of $z \sim 6$–8 observed in high-redshift LBGs, which have been attributed to their bursty star-formation histories and young stellar ages (H. Algera et al. 2026). In contrast, DSFGs likely experience less bursty star formation due to their longer depletion time-scales (M. Hagimoto et al. 2023) and more evolved stellar populations (E. da Cunha et al. 2015; S. Berta et al. 2023), naturally resulting in lower [O III] emission relative to their total star-formation rates. Moreover, [O III] emission can also be emitted because of interactions with ionizing particles and other ionization sources within multiphase gas reservoirs (K. C. Harrington et al. 2025). This could complicate the direct relation between the regions where [O III] is emitted and the dust emission, since this likely originates from star-forming and more extended, older stellar populations.

DSFGs are characterized by exceptionally high dust masses ($M_{\rm dust} \approx 10^{9-10}\ {\rm M}_\odot$; G. J. Bendo et al. 2023; M. Hagimoto et al. 2023; G. J. Bendo et al. 2025) resulting in optical depths that significantly exceed those of typical star-forming galaxies (H. S. B. Algera et al. 2024a, b). Since the observed dust masses of these HerBS sources approach $10^{11}\ {\rm M}_\odot$, even accounting for lensing, these sources are likely optically thick until 200 μm (C. M. Casey et al. 2018; T. Tsukui et al. 2023), and selective dust attenuation of [O III] could cause the lower ratios. Differential lensing, especially given the high magnification factors of these sources ($\mu > 4$; S. A. Urquhart et al. 2022) could also affect the line ratios (S. Serjeant 2012). Fig. C1 quantifies the effect of dust on lines and line ratios, showing that although optical depth can reduce the line-to-infrared ratio, the effect is up to ∼0.8 dex for a mixed medium. This would still place these DSFGs on the low side of the [O III]-to-infrared correlation, and suggests that the [O III] deficit is not simply a redshift evolution effect but reflects fundamental differences in the ionization structure of dusty versus UV-selected galaxies (cf. B. Peng et al. 2025c), with less dust-obscured galaxies likely having larger [O III]-emitting volumes surrounding star-forming regions. We note that this interpretation can be complicated by geometric effects. The high optical depths and irregular morphologies of DSFGs (T. J. L. C. Bakx et al. 2024c; J. A. Hodge et al. 2025) can create significant line-of-sight variations in extinction between lines, exacerbated by the stratified structure of photo-dissociation regions. [O III] emission from the innermost, most highly ionized zones could experience preferential extinction compared to [C II] and the bulk of the infrared emission from the outer, less-extinguished regions (L. Vallini et al. 2015). This effect is seen in observations (D. Cormier et al. 2019; M. Hagimoto et al. 2025) and simulations (D. Narayanan et al. 2015; C. C. Lovell et al. 2021) of high-redshift LBGs and local dwarf galaxies, with patchy, porous distributions of the

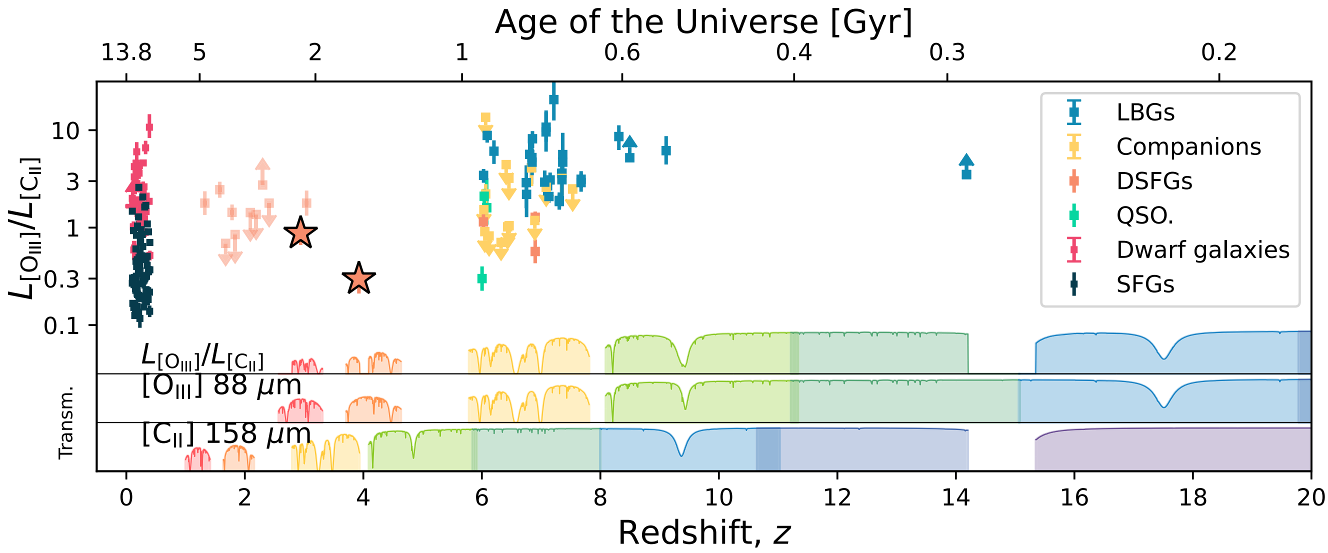

Figure 3. Oxygen-to-carbon line ratio ($L_{[\mathrm{O\,III}]}/L_{[\mathrm{C\,II}]}$) as a function of redshift from $z = 0$ to 15 showing the observational accessibility of these key diagnostic lines with ALMA. The upper panel displays the $L_{[\mathrm{O\,III}]}/L_{[\mathrm{C\,II}]}$ ratios measured in various galaxy populations across cosmic time, with our two DSFG sources with both [O III] and [C II] data (*orange stars*) showing low values compared to local dwarf galaxies (S. C. Madden et al. 2013; D. Cormier et al. 2015; P. Cigan et al. 2016; R. Ura et al. 2023), and in line with local spiral galaxies (T. Díaz-Santos et al. 2017) and *Herschel*/FTS-observed galaxies (Z.-Y. Zhang et al. 2018). The $L_{[\mathrm{O\,III}]}/L_{[\mathrm{C\,II}]}$ ratios of high-redshift LBGs (A. K. Inoue et al. 2016; S. Carniani et al. 2017, 2025; T. Hashimoto et al. 2018, 2019; N. Laporte et al. 2019; Y. Tamura et al. 2019; Y. Harikane et al. 2020; T. J. L. C. Bakx, S. Eales & A. Amvrosiadis 2020a; Y. Fudamoto et al. 2021; H. B. Akins et al. 2022; Y. Sugahara et al. 2022; J. Witstok et al. 2022; Y. H. V. Wong et al. 2022; Y. W. Ren et al. 2023; S. Fujimoto et al. 2024; L. E. Rowland et al. 2024; S. Schouws et al. 2025a, b; J. A. Zavala et al. 2024, 2025; H. S. B. Algera et al. 2024a; H. Algera et al. 2026), companion galaxies (B. P. Venemans et al. 2020; T. J. L. C. Bakx et al. 2024b; H. Algera et al. 2026), high-z DSFGs (D. P. Marrone et al. 2018; J. A. Zavala et al. 2018; K.-i. Tadaki et al. 2022), and quasar host galaxies (F. Walter et al. 2018; T. Hashimoto et al. 2019). The lower panel shows the atmospheric transmission for [O III] 88 μm and [C II] across ALMA's Bands, with the combined transmission indicating optimal redshift windows for simultaneous observations. The systematic [O III] deficit in DSFGs is observable across the full redshift range where both lines can be detected, suggesting this is a fundamental property of dusty star-forming environments rather than an observational bias.

neutral ISM, but hard to quantify without extensive, resolved observations.

We can rule out thermal saturation as the primary explanation for our observed line luminosities (cf. M. Rybak et al. 2019), as this would preferentially boost [O III] as more O^{++} ions become available. Similarly, an ISM substantially denser than the critical density ($n_{\mathrm{crit}} \gg 500\ \mathrm{cm}^{-3}$) could also result in similar results (cf. Y. Harikane et al. 2025; M. Usui et al. 2025; B. Peng et al. 2025a, b), but this would also affect the [C II] emission, with critical densities between $n_{\mathrm{crit}} = 50\ \mathrm{cm}^{-3}$ in ionized regions and $n_{\mathrm{crit}} = 2800\ \mathrm{cm}^{-3}$ in neutral regions (G. J. Stacey 2011). This agrees with gas densities estimated for HerBS-90 and -160 based on [C I]-to-infrared luminosity ratios (M. Hagimoto et al. 2023), indicating about 0.5 dex denser ISM for HerBS-160 ($10^{4.6}\ \mathrm{cm}^{-3}$ compared to $10^{4.1}\ \mathrm{cm}^{-3}$) but no significant variation in the [O III]-to-infrared luminosity ratio.

The implications for our understanding of DSFGs are significant. The [O III] deficit relative to other high-z galaxies suggests that, despite their extreme infrared luminosities, DSFGs are not the most extreme ionization environments in the high-redshift Universe. This supports models in which DSFGs represent a phase of galaxy evolution characterized by efficient star formation in gas-rich, metal-rich, and dusty environments. Consequently, the difference in stellar ages and star-formation modes between DSFGs and UV-selected galaxies contributes to the observed variation in ionization conditions. Future observations with higher sensitivity and angular resolution will be crucial for testing these interpretations, in particular using the upgraded ALMA capabilities in the Wideband Sensitivity Upgrade (J. Carpenter et al. 2023) and the future space mission PRIMA (J. Glenn et al. 2025). Spatially resolved [O III] maps could reveal whether the deficit reflects global properties or results from complex spatial distributions of ionizing sources and dust. Multiline diagnostics, including [N II] and [O I], can provide additional constraints on the ionization parameter, electron density, and chemical abundance patterns in these extreme environments.

ACKNOWLEDGEMENTS

The authors kindly thank Roberto Decarli for his insightful comments and suggestions to improve this manuscript. TB gratefully acknowledges financial support from the Knut and Alice Wallenberg Foundation through grant no. KAW 2020.0081. MH is supported by Japan Society for the Promotion of Science (JSPS) KAKENHI Grant No. 22H04939. LB and JGN acknowledge the CNS2022-135748 project and the PID2021-125630NB-I00 project. PP is a member of the International Max Planck Research School (IMPRS∗) in Astronomy and Astrophysics. PP, DR, and AW acknowledge the Collaborative Research Center 1601 (SFB 1601 sub-project C2) funded by the Deutsche Forschungs Gemeinschaft (DFG, German Research Foundation) – 500700252. HSBA acknowledges support from Academia Sinica through grant AS-PD-1141-M01-2. We are grateful to Dominik Riechers for the useful discussions. This paper makes use of the following ALMA data: ADS/JAO.ALMA 2021.1.00265.S, 2022.1.00145.S, 2022.1.00432.S, and 2023.1.00750.S.

DATA AVAILABILITY

The data sets are available on the ALMA Science Archive and generated using the standard data calibration protocols.

REFERENCES

Akins H. B. et al., 2022, ApJ, 934, 64
Algera H. et al., 2026, MNRAS, 545, staf1897
Algera H. S. B. et al., 2024a, MNRAS, 527, 6867
Algera H. S. B. et al., 2024b, MNRAS, 533, 3098
Bakx T. J. L. C. et al., 2018, MNRAS, 473, 1751
Bakx T. J. L. C., Eales S., Amvrosiadis A., 2020a, MNRAS, 493, 4276
Bakx T. J. L. C. et al., 2020b, MNRAS, 494, 10
Bakx T. J. L. C. et al., 2023, MNRAS, 519, 5076
Bakx T. J. L. C., Gray B. S., González-Nuevo J., Bonavera L., Amvrosiadis A., Eales S., Hagimoto M., Serjeant S., 2024a, MNRAS, 527, 8865
Bakx T. J. L. C. et al., 2024b, MNRAS, 532, 2270
Bakx T. J. L. C. et al., 2024c, MNRAS, 535, 1533
Baryshev A. M. et al., 2015, A&A, 577, A129
Bendo G. J. et al., 2023, MNRAS, 522, 2995
Bendo G. J. et al., 2025, MNRAS, 540, 1560
Berta S. et al., 2023, A&A, 678, A28
Blain A. W., Smail I., Ivison R. J., Kneib J. P., Frayer D. T., 2002, Phys. Rep., 369, 111
Carilli C. L., Walter F., 2013, ARA&A, 51, 105
Carniani S. et al., 2017, A&A, 605, A42
Carniani S. et al., 2025, A&A, 696, A87
Carpenter J., Brogan C., Iono D., Mroczkowski T., 2023, in V. Ossenkopf-Okada et al., eds, Physics and Chemistry of Star Formation: The Dynamical ISM Across Time and Spatial Scales. Universitäts- und Stadtbibliothekj Köln, Köln, p. 304
CASA Team, 2022, PASP, 134, 114501
Casey C. M., Narayanan D., Cooray A., 2014, Phys. Rep., 541, 45
Casey C. M. et al., 2018, ApJ, 862, 77
Cigan P. et al., 2016, AJ, 151, 14
Cormier D. et al., 2015, A&A, 578, A53
Cormier D. et al., 2019, A&A, 626, A23
Cox P. et al., 2023, A&A, 678, A26
da Cunha E. et al., 2015, ApJ, 806, 110
Daddi E. et al., 2015, A&A, 577, A46
Dannerbauer H., Daddi E., Riechers D. A., Walter F., Carilli C. L., Dickinson M., Elbaz D., Morrison G. E., 2009, ApJ, 698, L178
Decarli R., Díaz-Santos T., 2025, A&AR, 33, 4
Decarli R. et al., 2023, A&A, 673, A157
Díaz-Santos T. et al., 2017, ApJ, 846, 32
Eales S. et al., 2010, PASP, 122, 499
Ferkinhoff C., Hailey-Dunsheath S., Nikola T., Parshley S. C., Stacey G. J., Benford D. J., Staguhn J. G., 2010, ApJ, 714, L147
Ferrara A., Vallini L., Pallottini A., Gallerani S., Carniani S., Kohandel M., Decataldo D., Behrens C., 2019, MNRAS, 489, 1
Fudamoto Y. et al., 2021, Nature, 597, 489
Fujimoto S. et al., 2024, ApJ, 964, 146
Glenn J. et al., 2025, J. Astron. Telesc. Instrum. Syst., 11, 031628
Hagimoto M. et al., 2023, MNRAS, 521, 5508
Hagimoto M. et al., 2025, ApJ, 990, 29
Harikane Y. et al., 2020, ApJ, 896, 93
Harikane Y. et al., 2025, ApJ, 993, 204
Harrington K. C. et al., 2021, ApJ, 908, 95
Harrington K. C., Vishwas A., Man A. W. S., De Breuck C., Papadopoulos P. P., Andreani P., Bisbas T. G., 2025, 2025, 701, 298
Hashimoto T. et al., 2018, Nature, 557, 392
Hashimoto T., Inoue A. K., Tamura Y., Matsuo H., Mawatari K., Yamaguchi Y., 2019, PASJ, 71, 109
Herrera-Camus R. et al., 2018, ApJ, 861, 94
Hodge J. A., da Cunha E., 2020, R. Soc. Open Sci., 7, 200556
Hodge J. A. et al., 2013, ApJ, 768, 91
Hodge J. A. et al., 2019, ApJ, 876, 130
Hodge J. A. et al., 2025, ApJ, 978, 165
Högbom J. A., 1974, A&AS, 15, 417
Inami H. et al., 2022, MNRAS, 515, 3126
Inoue A. K. et al., 2016, Science, 352, 1559
Karim A. et al., 2013, MNRAS, 432, 2
Laporte N. et al., 2017, ApJ, 837, L21
Laporte N. et al., 2019, MNRAS, 487, L81
Lovell C. C., Geach J. E., Davé R., Narayanan D., Li Q., 2021, MNRAS, 502, 772
Madau P., Dickinson M., 2014, ARA&A, 52, 415
Madden S. C. et al., 2013, PASP, 125, 600
Maddox S. J. et al., 2018, ApJS, 236, 30
Marrone D. P. et al., 2018, Nature, 553, 51
Nakajima K., Ouchi M., Isobe Y., Harikane Y., Zhang Y., Ono Y., Umeda H., Oguri M., 2023, ApJS, 269, 33
Narayanan D. et al., 2015, Nature, 525, 496
Neri R. et al., 2020, A&A, 635, A7
Oliver S. J. et al., 2012, MNRAS, 424, 1614
Olsen K., Greve T. R., Narayanan D., Thompson R., Davé R., Niebla Rios L., Stawinski S., 2017, ApJ, 846, 105
Pearson E. A. et al., 2013, MNRAS, 435, 2753
Peng B., Lamarche C., Ball C., Vishwas A., Stacey G., Rooney C., Nikola T., Ferkinhoff C., 2025a, preprint (arXiv:2507.10702)
Peng B., Vishwas A., Lamarche C., Stacey G., Ball C., Rooney C., Nikola T., Ferkinhoff C., 2025b, preprint (arXiv:2507.11829)
Peng B., Stacey G., Vishwas A., Ball C., Lamarche C., Rooney C., Nikola T., Ferkinhoff C., 2025c, preprint (arXiv:2507.12896)
Planck Collaboration VI, 2020, A&A, 641, A6
Prajapati P. et al., 2026, ApJS, 282, 40
Remijan A. et al., 2019, ALMA Technical Handbook, ALMA Doc. 7.3, ver. 1.1, 2019, ISBN 978-3-923524-66-2, doi:10.5281/zenodo.4511522
Ren Y. W. et al., 2023, ApJ, 945, 69
Reuter C. et al., 2020, ApJ, 902, 78
Rizzo F., Vegetti S., Powell D., Fraternali F., McKean J. P., Stacey H. R., White S. D. M., 2020, Nature, 584, 201
Rizzo F. et al., 2024, A&A, 689, A273
Rowland L. E. et al., 2024, MNRAS, 535, 2068
Rowland L. E. et al., 2026, MNRAS, tmp, 14
Rybak M. et al., 2019, ApJ, 876, 112
Rybak M. et al., 2022, A&A, 667, A70
Schouws S. et al., 2022, ApJ, 928, 31
Schouws S. et al., 2025a, ApJ, 988, 19
Schouws S. et al., 2025b, preprint (arXiv:2502.01610)
Serjeant S., 2012, MNRAS, 424, 2429
Shivaei I. et al., 2018, ApJ, 855, 42
Simpson J. M. et al., 2019, ApJ, 880, 43
Smail I. et al., 2021, MNRAS, 502, 3426
Solomon P. M., Vanden Bout P. A., 2005, ARA&A, 43, 677
Stacey G. J., 2011, IEEE Trans. Terahertz Sci. Technol., 1, 241
Sugahara Y., Inoue A. K., Fudamoto Y., Hashimoto T., Harikane Y., Yamanaka S., 2022, ApJ, 935, 119
Sun F. et al., 2025, preprint (arXiv:2506.06418)
Tacconi L. J. et al., 2008, ApJ, 680, 246
Tadaki K.-i. et al., 2022, PASJ, 74, L9
Tadaki K., Esposito F., Vallini L., Tsukui T., Saito T., Iono D., Michiyama T., 2025, Nat. Astron., 9, 720
Tamura Y. et al., 2019, ApJ, 874, 27
Tsukui T., Wisnioski E., Krumholz M. R., Battisti A., 2023, MNRAS, 523, 4654
Tsukui T., Wisnioski E., Bland-Hawthorn J., Mai Y., Iguchi S., Baba J., Freeman K., 2024, MNRAS, 527, 8941
Ura R. et al., 2023, ApJ, 948, 3
Urquhart S. A. et al., 2022, MNRAS, 511, 3017
Usui M. et al., 2025, ApJL, 991, L38
Uzawa Y. et al., 2013, Phys. C Supercond., 494, 189
Valiante E. et al., 2016, MNRAS, 462, 3146
Vallini L., Gallerani S., Ferrara A., Pallottini A., Yue B., 2015, ApJ, 813, 36

Vallini L., Ferrara A., Pallottini A., Carniani S., Gallerani S., 2021, MNRAS, 505, 5543
van der Werf P. P. et al., 2010, A&A, 518, L42
van Leeuwen I. F. et al., 2025, MNRAS, 542, 1388
Venemans B. P. et al., 2020, ApJ, 904, 130
Walter F. et al., 2018, ApJ, 869, L22
Ward B. A. et al., 2022, MNRAS, 510, 2261
Witstok J. et al., 2022, MNRAS, 515, 1751
Wong Y. H. V. et al., 2022, ApJ, 929, 161
Zavala J. A. et al., 2018, Nat. Astron., 2, 56
Zavala J. A. et al., 2021, ApJ, 909, 165
Zavala J. A. et al., 2024, ApJ, 977, L9
Zavala J. A. et al., 2025, Nat. Astron., 9, 155
Zhang Z.-Y. et al., 2018, MNRAS, 481, 59

APPENDIX A: ACA OBSERVATION SET-UPS

Table A1 provides the details of the ACA observations.

Table A1. Parameters of the ACA observations.

UTC end time	Frequency (GHz)	T_{int} (min)	PWV (mm)
	HerBS-28		
2024-08-10 07:26:44	688.930	124.16	0.47
2024-07-13 10:42:43	688.930	123.83	0.15
2024-06-06 12:27:26	688.930	123.47	0.70
	HerBS-90		
2024-09-09 08:58:49	679.670	118.86	0.49
2024-09-08 11:03:45	679.670	122.87	0.28
2024-09-08 09:00:40	679.670	118.66	0.30
	HerBS-103		
2024-09-27 07:57:49	860.732	123.30	0.25
2024-09-27 05:54:26	860.732	123.34	0.24
2024-09-22 06:25:41	860.732	122.65	0.48
2024-09-21 06:14:25	860.732	122.73	0.58
	HerBS-160		
2024-07-04 13:39:02	684.764	122.55	0.47
2024-06-07 13:15:31	684.764	123.03	1.01
2023-11-03 06:09:25	684.764	123.48	0.39

Note. Col. 1: UTC end time of the observations as (YYYY-MM-DD hh:mm:ss). Col. 2: The observed frequency. Col. 3: The total observation time including overheads. Col. 4: The precipitable water vapour during the observations.

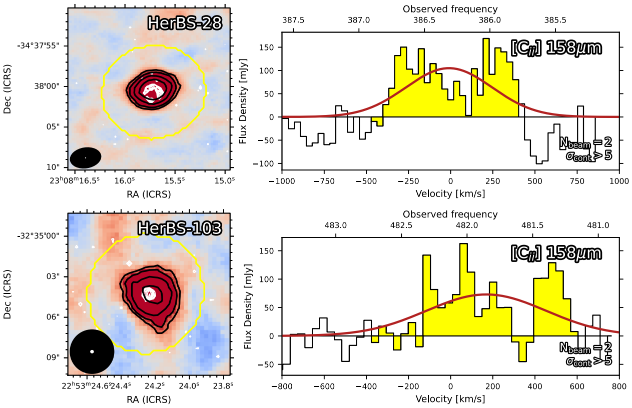

Figure B1. [C II] spectra of HerBS-28 and -103, similar to Fig. 1. The poststamps show the 12 arcsec by 12 arcsec moment-0 map of the [C II] 158 μm emission line as the background and black contours at 2σ, 3σ, 5σ starting at ±2, centred on the positions listed in Table 1. The white contour indicates the high-resolution Band 7 continuum data (T. J. L. C. Bakx et al. 2024c), which is used as the basis for the aperture as shown in *yellow contours* for the spectrum shown on the right-hand side.

APPENDIX B: IONIZED CARBON EMISSION OF HERBS-28 AND -103

Fig. B1 shows the [C II] spectra of HerBS-28 and -103, produced through the same process as the [O III] spectra discussed in this paper.

APPENDIX C: DUST ATTENUATION OF LINE RATIOS

Following the prescriptions as detailed in R. Decarli et al. (2023), H. S. B. Algera et al. (2024a), and K. Tadaki et al. (2025), we estimate the effect of dust attenuation on line fluxes and ratios as follows. The optical depth τ_λ at a given wavelength λ relative to the transitional wavelength λ_{thick} is $\tau_\lambda = (\lambda/\lambda_{\mathrm{thick}})^{-\beta}$, where β is the dust emissivity index assumed to be $\sim$2 in line with most observations of DSFGs (G. J. Bendo et al. 2023, 2025). The subsequent transmission is calculated as $F_{\mathrm{obs.}}/F_{\mathrm{intr.}} = (1 - e^{-\tau_\lambda})/\tau_\lambda$.

Fig. C1 shows the absolute transmission of lines and relative attenuation of line ratios at different frequencies as a function of the transition wavelength. The absolute transmission of [O III] drops from 1 to 0.19 at $\lambda_{\mathrm{thick}} = 200$ μm. The ratio varies between 1 (no effect of dust attenuation) and $(\lambda_1/\lambda_2)^{\beta}$ in the optically thick case. For $L_{[\mathrm{O\,III}]}/L_{[\mathrm{C\,II}]}$, this means a maximum dust effect of 31 per cent on the line ratio, with 69 per cent preferential absorption in

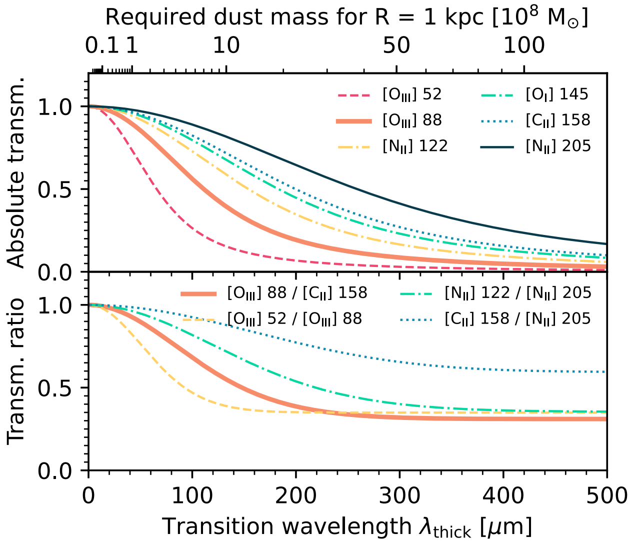

Figure C1. The dust attenuation affects line ratios differently for a varying transitional absorption wavelength $\lambda_{\rm thick}$. The ratio varies between 1 (no effect of dust attenuation) and $(\lambda_1/\lambda_2)^\beta$ in the optically thick case. Assuming Milky Way dust properties, a spherical dust distribution, and $\beta_{\rm dust} = 2$, the required dust mass to achieve a transition wavelength is shown in the top x-axis.

the [O III] 88 μm relative to the [C II] 158 μm. Using equation 6 from H. S. B. Algera et al. (2024a),[3] we scale the transition wavelength to a total required dust mass, presuming Milky Way dust mass absorption coefficient and a typical dust reservoir size of 1 kpc.

[1] *Department of Space, Earth and Environment, Chalmers University of Technology, SE-412 96 Gothenburg, Sweden*
[2] *Institute of Astronomy and Astrophysics, Academia Sinica, 11F of Astronomy-Mathematics Building, No. 1, Section 4, Roosevelt Rd, Taipei 106319, Taiwan, R.O.C.*
[3] *I. Physikalisches Institut, Universität zu Köln, Zülpicher Strasse 77, D-50937 Köln, Germany*
[4] *Max-Planck-Institut für Radioastronomie, Auf dem Hügel 69, D-53121 Bonn, Germany*
[5] *UK ALMA Regional Centre Node, Jodrell Bank Centre for Astrophysics, Department of Physics and Astronomy, University of Manchester, Oxford Road, Manchester M13 9PL, UK*
[6] *Institut de Radioastronomie Millimétrique (IRAM), 300 Rue de la Piscine, F-38400 Saint-Martin-d'Hères, France*
[7] *Departamento de Fisica, Universidad de Oviedo, C. Federico Garcia Lorca 18, E-33007 Oviedo, Spain*
[8] *Instituto Universitario de Ciencias y Tecnologas Espaciales de Asturias (ICTEA), C. Independencia 13, E-33004 Oviedo, Spain*
[9] *Institut d'Astrophysique de Paris, Sorbonne Université, UPMC Université Paris 6 and CNRS, UMR 7095, 98 bis boulevard Arago, F-75014 Paris, France*
[10] *Department of Physics, Graduate School of Science, Nagoya University, Aichi 464-8602, Japan*
[11] *Joint ALMA Observatory, Alonso de Córdova 3107, Vitacura, Casilla 19001, Santiago de Chile, Chile*
[12] *National Astronomical Observatory of Japan, Los Abedules 3085 Oficina 701, Vitacura 7630414, Santiago, Chile*
[13] *European Southern Observatory, Alonso de Córdova 3107, Vitacura, Casilla 19001, Santiago de Chile, Chile*
[14] *Instituto de Estudios Astrofísicos, Facultad de Ingeniería y 455 Ciencias, Universidad Diego Portales, Av. Ejército Libertador 441, Santiago, Chile*
[15] *Université Lyon 1, ENS de Lyon, Centre de Recherche Astrophysique de Lyon (UMR5574), F-69230 Saint-Genis-Laval, France*
[16] *School of Physical Sciences, The Open University, Milton Keynes MK7 6AA, UK*
[17] *Astrophysics Branch, NASA – Ames Research Center, MS 245-6, Moffett Field, CA 94035, USA*
[18] *Leiden Observatory, Leiden University, PO Box 9513, NL-2300 RA Leiden, the Netherlands*
[19] *INAF, Osservatorio Astronomico di Padova, Vicolo Osservatorio 5, I-35122 Padova, Italy*

This paper has been typeset from a TEX/LATEX file prepared by the author.

---

[3] $\lambda_{\rm thick} \approx 42\ \mu{\rm m} \times (R\,[{\rm kpc}])^{-1} \times (M_{\rm dust}\,[10^8\,{\rm M}_\odot])^{1/2}$.